Highly efficient and eco-friendly green quantum dot light-emitting diodes through interfacial potential grading

Yuhe Bi [1], Jianhui Sun[2], Sheng Cao [1] ✉, Qiuyan Li[1], Jinju Zheng[3], Xi Yuan[4], Yunjun Wang [5] ✉, Bingsuo Zou [1,6] ✉ & Jialong Zhao [1] ✉

As next-generation display technologies, eco-friendly colloidal quantum dot light-emitting diodes have drawn great attention due to their excellent luminescence properties, along with their rapid development. However, practical applications of eco-friendly quantum dot light-emitting device remain challenging, primarily due to the inferior performance of green device, which still lag behind their red and blue counterparts. Herein, we present efficient green device based on interfacial potential-graded ZnSeTe quantum dots. Our findings show that this potential-graded structure alleviates interfacial lattice mismatch and strain, reducing structural deformation and misfit defects. The smoothed interfacial potential suppresses the nonradiative recombination processes, particularly Auger recombination revealed by excitation-intensity dependent ultrafast transient absorption kinetics. Consequently, the interfacial potential-graded quantum dots demonstrate highly efficient green quantum dot light-emitting diodes, with a peak external quantum efficiency of 21.7% at 520 nm and a corresponding current efficiency of 75.7 cd A^{-1}.

Quantum dot light-emitting diodes (QLEDs) are commonly seen as crucial contenders for next-generation display and lighting technologies[1–6], owing to their exceptional luminescence properties and low production costs. Over the past decade, significant progress has been made in cadmium (Cd) selenide and lead (Pb) halide perovskite-based QLEDs[7–16]. Recently, heavy-metal-free indium phosphide (InP) and zinc selenide-telluride (ZnSeTe) quantum dot (QD)-based QLEDs have emerged as a more sustainable alternative for display applications and have demonstrated promising performance[17–22]. For instance, red InP-based QLEDs and blue ZnSeTe-based QLEDs have reached external quantum efficiency (EQE) of 21.4% and 20.2%, respectively, having long lifetimes—615 h at 1000 cd m^{-2} for T_{95} (the time when the luminance decreases to 95% of its original value) and

442 h at 650 cd m^{-2} for T_{50} (the time when the luminance decreases to 50% of its original value)[17,19]. Notably, recent advancements in green InP-based QLEDs have demonstrated a high EQE of 26.68% and a T_{95} lifetime of 1241 h (at 1000 cd m^{-2})[18]. These developments, particularly those led by Shen et al., represent a significant step forward. However, despite these advancements, most reported green InP and ZnSeTe QLEDs continue to lag behind their red and blue counterparts[20,23–28]. For instance, the maximum EQE of green ZnSeTe-based QLEDs at just 10.1%, with a T_{50} lifetime of only 52 h at 1000 cd m^{-2}. This disparity in performance has impeded the balanced development and practical utilization of heavy-metal-free red, green, and blue QLEDs. Since the human eye is highly sensitive to the green spectral region[29], resolving this performance gap to develop efficient and bright green QLEDs is

[1]School of Physical Science and Technology, State Key Laboratory of Featured Metal Materials and Life-cycle Safety for Composite Structures, Guangxi University, Nanning, China. [2]College of Physics Science and Technology, Heilongjiang University, Harbin, China. [3]Institute of Micro/Nano Materials and Devices, Ningbo University of Technology, Ningbo, China. [4]College of Information Technology, Jilin Engineering Research Center of Optoelectronic Materials and Devices, Jilin Normal University, Siping, China. [5]Suzhou Xingshuo Nanotech Co. Ltd. (Mesolight), Suzhou, China. [6]School of Resources, Environment and Materials, Guangxi Key Laboratory of Processing for Non-Ferrous Metals and Featured Materials, Guangxi University, Nanning, China. ✉e-mail: caosheng@gxu.edu.cn; yjwt@mesolight.cc; zoubs@gxu.edu.cn; zhaojl@gxu.edu.cn

essential for the technological advancement and to fully realize its potential in display and lighting applications.

Research on heavy-metal-free green QLEDs currently focuses on QDs based on either InP or ZnSeTe[18,20,23,27,28]. InP QDs encounter substantial hurdles because of their narrow bulk bandgap (1.35 eV) and large excitonic Bohr radius (10.0 nm)[30]. Smaller cores are required for green emission, and the synthesis of high-quality green QDs with core/shell structures is thus complicated[31,32]. Additionally, InP has been classified as a Group 2A carcinogen by the World Health Organization[33], raising concerns about its safety and suitability as an eco-friendly emitter in QLEDs. In contrast, ZnSeTe QDs show potential as eco-friendly green emitters due to their band-gap-bowing properties[27,28,34], enabling precise tuning of emission wavelengths through alloy composition and quasi-type II heterostructure. However, achieving green emission in ZnSeTe QDs requires a significant amount of Te, which results in a larger lattice mismatch at the core/shell interface compared to blue ZnSeTe QDs. This leads to a substantial interfacial potential difference between core and shell[28,35], increasing Auger recombination rates and drastically reducing device efficiency, particularly at high brightness levels. Currently, there is no effective solution to mitigate Auger recombination in green ZnSeTe QLEDs[26–28]. While progress has been made in suppressing Auger recombination in Cd-based and InP-based QDs by smoothing interfacial potential[31,32,36,37], the relationship between interfacial potential and the performance of ZnSeTe QDs in QLEDs remains unclear. These unresolved challenges keep continue to hinder the development of high-performance green ZnSeTe QLEDs.

In this work, we report highly efficient, eco-friendly green QLEDs enabled by tailoring the interfacial potential structure of ZnSeTe QDs. The interfacial potential is controlled by the growth of graded Te distribution core/shell structure, resulting in an interfacial potential-graded (IPG) structure, referred to as IPG QDs. We demonstrate that the IPG QDs possess a compositional gradient alloyed heterostructure, which significantly enhances their luminescent properties. Lattice vibration analysis of the longitudinal optical (LO) phonon mode confirms that compressive strain in the QD core is reduced with the IPG configuration. Furthermore, ultrafast exciton dynamic analysis reveals a notable reduction in nonradiative Auger recombination in IPG QDs compared to control QDs. As a result, the IPG QDs achieve a photoluminescence (PL) quantum yield (QY) of up to 95%, with a narrow linewidth of 38 nm. Green ZnSeTe QLEDs based on IPG QDs demonstrate a peak EQE of 21.7%, a peak current efficiency of 75.7 cd A^{-1}, and a T_{50} lifetime of 99.4 h at 1000 cd m^{-2}. This work successfully addresses the performance limitations in green ZnSeTe QLEDs and provides deep insights into the relationship between interfacial confinement potential and QLEDs performance, advancing the development of high-performance, eco-friendly green QLEDs.

Results

Design and structure characterization

To achieve green light emission from ZnSeTe-based QDs, we tailor the Te content in the ZnSeTe QD cores to a Te/Se ratio of 1:4, leveraging the bandgap bowing properties of ternary alloys. Previous studies have shown that increasing the Te content enhances the lattice mismatch between the ZnSeTe core and the ZnSe shell, which amplifies the potential distribution at the core-shell interface[34,35]. This leads to a steep interfacial potential that induces Auger recombination, reducing luminescence efficiency[31]. To address this issue, we introduce an IPG shell between the ZnSeTe core and the ZnSe shell (as demonstrated in Supplementary Figs. 1 and 2). The designed QD structure and the corresponding interfacial potential are depicted in Fig. 1a, while the synthesis schematic of the IPG QDs is shown in Fig. 1b.

We first synthesize the green ZnSe$_{0.8}$Te$_{0.2}$ QD cores at 240 °C (referred to Stage 1), and then passivate the surface defects with HF/ZnCl$_2$, using a method successfully demonstrated in InP and ZnSeTe

QDs. Next, we grow the ZnSe$_{0.9}$Te$_{0.1}$ IPG shell at 280 °C (Stage 2, core/IPG). Finally, the QDs are sequentially coated with a ZnSe shell (Stage 3) and a ZnS shell (Stage 4), as shown in Fig. 1b. For the control QDs, we directly coat the ZnSe$_{0.8}$Te$_{0.2}$ QD cores with a ZnSe shell of the same thickness instead of IPG shell, while keeping the other shells the same, to ensure that size-related factors are consistent between samples (detailed synthesis methodology is shown in the experimental section).

X-ray diffraction (XRD) patterns (Fig. 1c, d) show that all diffraction peaks match the standard blende (ZB) ZnSe pattern (JCPDS No. 37-1463), confirming that both QD types maintained a ZB crystal structure without the emergence of the wurtzite (WZ) structure. This is likely due to the effective elimination of stacking faults in the ZnSe shell using HF during synthesis[19]. As the ZnSe or ZnS shell layers are applied, both the IPG QDs and the control QDs exhibited improved crystallization, as indicated by the sharpening of diffraction peaks, a slight red shift, and the narrowing of the peak line widths.

To verify the IPG structure of the green ZnSeTe alloy QDs, high-angle annular dark-field (HAADF) scanning transmission electron microscopy (STEM) and energy dispersive spectroscopy (EDS) elemental mapping are used to examine the morphology and composition distribution of QDs (Fig. 1e, f). The IPG QDs exhibit a well-defined cubic shape, while the control QDs display an irregular shape (Fig. 1g, h), likely due to greater structure deformation caused by increased lattice strain between the core and ZnSe shell[38]. EDS analysis indicate that the Te distribution in the control QDs is more inhomogeneous compared to the IPG QDs (full EDS data available in Supplementary Figs. 3 and 4). In traditional ZnSeTe/ZnSe core/shell structure, the heavy Te alloying in the ZnSeTe core increases lattice strain and interlayer mismatch[34,35]. The inhomogeneous Te distribution in the control QDs can be attributed to the increased interlayer mismatch, which enhances compressive stress on the core as the shell thickness increases, leading to a partially aggregated distribution of Te within the core. Furthermore, element line scanning of the Se and Te atomic fractions directly reveal the interface component changes and core/shell structure. As shown in Fig. 1i, j, the Te distribution in the control QDs exhibit a steep transition, whereas in the IPG QDs, the Te distribution shows a gradual gradient along the radius. These results confirm that the IPG shell is epitaxially grown on the ZnSeTe core, resulting in the formation of a graded interfacial potential in the target IPG QDs.

Optical property and growth process characterization

To investigate the effects of IPG structure on luminescence performance, we record the absorption and PL spectra at each synthesis stage (Fig. 2a, b), along with the PL QY of QDs (Fig. 2c, d). Due to the quasi-type II heterostructure of ZnSeTe/ZnSe, electrons can delocalize across the shell[22,34]. As a result, the PL peak shifts from 463 nm (for the cores) to 515 nm (for the control QDs) and 519 nm (for the IPG QDs) with the coating of ZnSe/ZnS shells (Fig. 2a, b). The 4 nm red shift observed in IPG QDs compared to the control QDs is attributed to carrier wavefunction delocalization, which is induced by the IPG structure and the effect of Te in the shell. In the control QDs, the hole wavefunction is strongly confined within the core. However, the introduction of the IPG leads to a stronger leakage of the carrier wave function outside the core. In the IPG QDs, the hole wavefunction becomes more delocalized due to the gradient potential, as shown in the inset of Fig. 2e. This delocalization results in a lower confinement of the hole, causing the red shift in the PL peak[31]. Additionally, the presence of Te in the shell further affects the band structure, contributing to the redshift.

The QDs grow in size from stage 1 (cores, 3.1 nm) to stage 4 (8.7 nm for control QDs, 8.8 nm for IPG QDs). Transmission electron microscopy (TEM) images of QDs at each stage (size distribution of
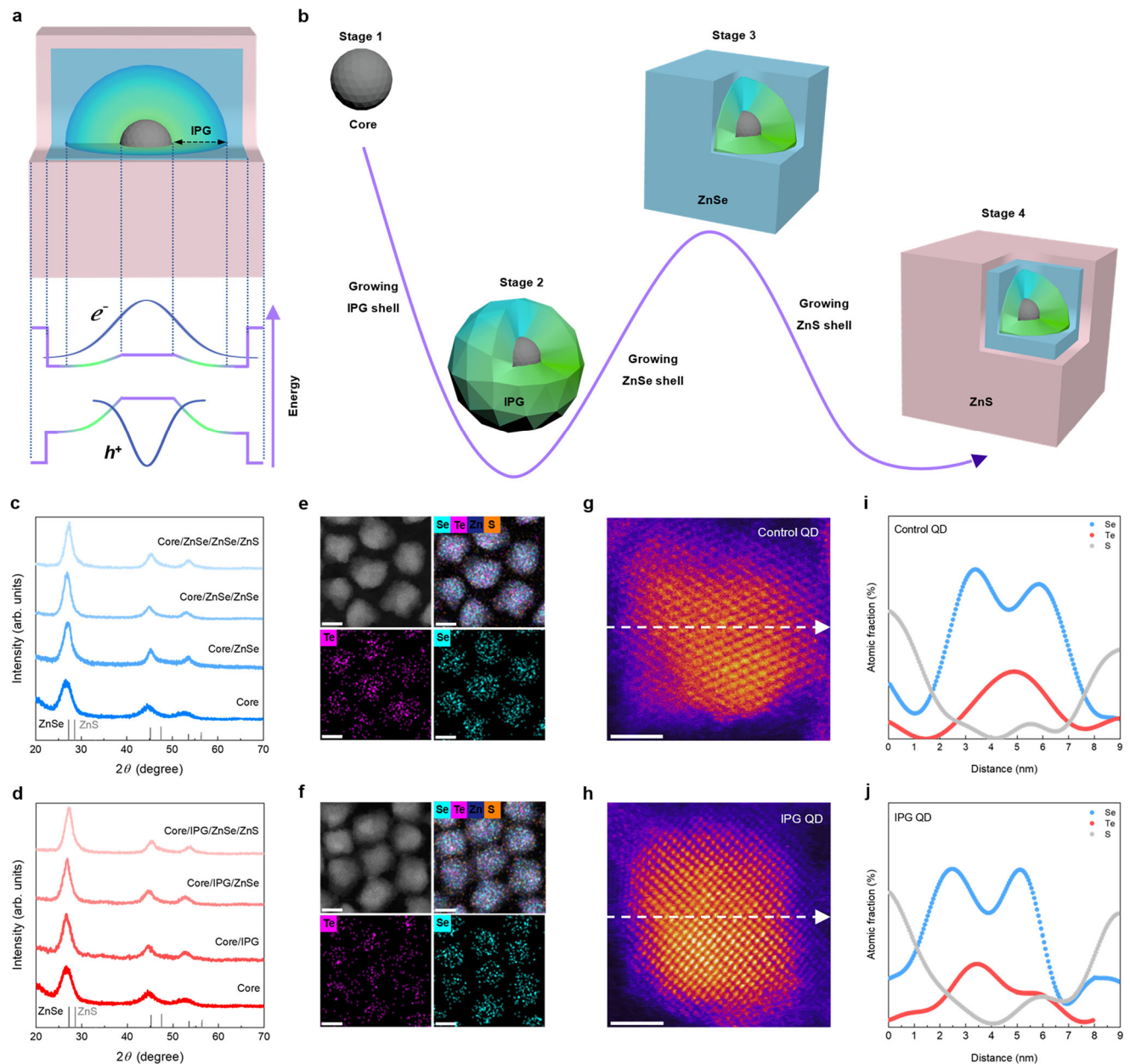
Fig. 1 | Schematic illustration and structure characterization. a Schematic illustration of the IPG QDs and interfacial potential structure. **b** Synthesis schematic of core/IPG/ZnSe/ZnS QDs. **c, d** XRD patterns of control and IPG QDs at each stage. **e, f** HAADF STEM image and EDS elemental mapping of control and IPG QDs. The scale bar is 5 nm. **g, h** HAADF STEM image of signal control and IPG QD. The scale bar is 2 nm. **i, j** Smoothed EDS line scanning profiles of the corresponding signal control and IPG QD along dotted arrow.

QDs at all stages is shown in Supplementary Figs. 5 and 6) are presented alongside the corresponding PL spectra. At stage 2, both the IPG and ZnSe shells are 1.0 nm thick for IPG QDs and control QDs. For stages 3 and 4, the thickness of ZnSe and ZnS shells is measured to be 1.0 nm and 0.8 nm, respectively, for both types of QDs. TEM images reveal that the core/IPG QDs in stage 2 exhibit a uniformly distributed spherical shape, while the core/ZnSe QDs become increasingly irregular in shape, especially after the ZnSe (stage 3) and ZnS (stage 4) shell coatings (Fig. 2a, b). This intensified structure deformation is attributed to the large interfacial potential and lattice strain between the ZnSe shell and ZnSeTe core, where heavy-Te alloying significantly narrows the optical band gap (E_g)[28,35]. As the shells are applied, the PL QY of IPG QDs increases dramatically from less than 6% at stage 1 to 95% at stage 4, while the PL QY of control QDs only reaches 70% (Fig. 2c, d). Concurrently, the full width at half-maximum (FWHM) of

the PL decreases from 53 nm (cores) to 38 nm (IPG QDs) and 47 nm (control QDs). It has been reported that the large lattice mismatch between the core and shell generates increased lattice strain, applying compressive stress to the core[38,39]. This stress induces misfit defects and structure deformation at the interface, ultimately degrading luminescence performance. Therefore, the significant improvement in PL QY and the reduction in FWHM in IPG QDs can be attributed to the reduced interfacial strain and the suppression of interfacial defects.

To further validate the role of the IPG structure in enhancing luminescence, we perform time-resolved PL spectroscopy (Fig. 2e, f) on the QDs. The PL dynamics are analyzed using a triexponential function, with the fitting results provided in Supplementary Table 1. We observe that the average lifetime (τ_{av}) increases from 21.6 ns in stage 1 (cores) to 58.3 ns in stage 4 (control QDs) and 70.3 ns in stage 4 (IPG QDs). This increase is attributed to the enhanced exciton
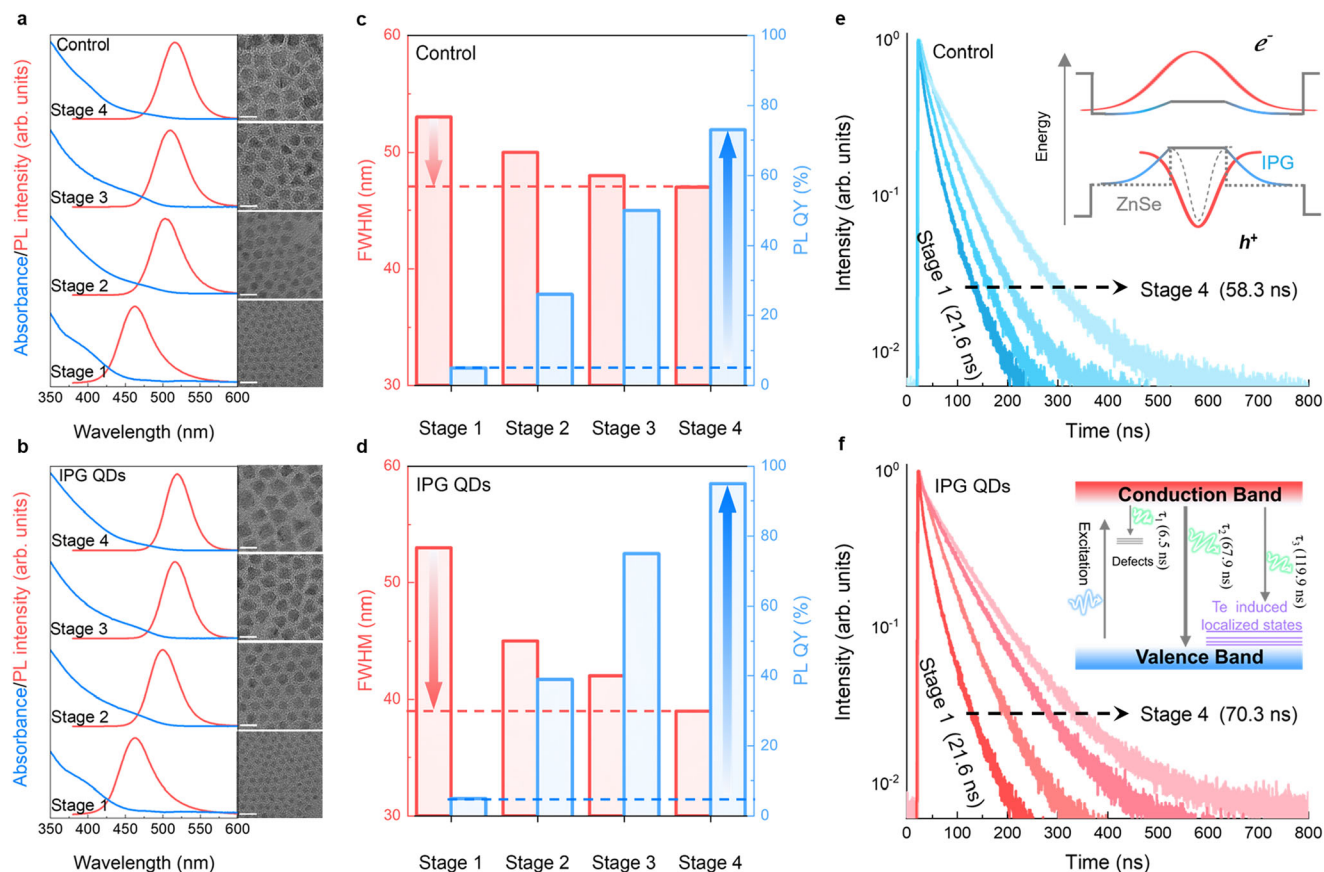
Fig. 2 | Luminescence and structure characteristics for control and IPG QDs. a, **b** PL and absorption spectra of control and IPG QDs at each stage. The corresponding TEM images are shown on the right side. The scale bar is 10 nm. **c**,**d** The FWHM and PL QY of control and IPG QDs at each stage. **e**, **f** Time-resolved PL spectra of control QDs (inset: schematic energy level diagram of delocalized electron wavefunction and localized hole wavefunction for IPG QDs (red solid line) and control QDs (gray dotted line)), and IPG QDs (inset: schematic energy level diagram of radiative and non-radiative transition pathways, where τ_1, τ_2, and τ_3 represents the lifetime of defect-assisted recombination, band-edge recombination and localized state recombination of IPG QDs, respectively) at each stage.

delocalization and the suppression of nonradiative recombination due to the successive growth of multiple shell layers.

The PL dynamic is strongly influenced by the Te content, which can lead to localized hole states at the top of valence band and affect the recombination processes. The fast decay components are likely associated with nonradiative defect-assisted recombination[40–44], while the slow decay components are related to the recombination of localized hole states[45–48] (as shown in inset of Fig. 2f). Specifically, the amplitude of the fast decay components in the cores is 0.43, decreasing to 0.26 for control QDs and 0.17 for IPG QDs as additional shell layers are coated. The reduction in the fast decay component amplitude represents a decrease in nonradiative recombination, which is inversely proportional to the PL QY[22,40,43]. The coating of ZnSe/ZnS shell effectively passivates interfacial defects and reduces nonradiative recombination pathways, which directly contributes to the dramatic improvement in PLQY from less than 6% at Stage 1 to 95% at Stage 4. The suppression of the fast decay component in IPG QDs indicates that defect-assisted nonradiative recombination is significantly minimized, likely due to minimized interfacial strain in the IPG structure.

Lattice strain and ultrafast carrier dynamics

To further explore the effects of interfacial potential on lattice strain of ZnSeTe alloy QDs, we conduct Raman spectroscopy measurements[38]. Figure 3a, b shows the Raman spectra of both IPG and control QDs, revealing asymmetric fundamental Raman peak around 240 cm^{-1}. These spectra are deconvoluted into three Lorentzian peaks (fitting results are shown in Supplementary Table 2), corresponding to transversal optical (TO) phonons (~200 cm^{-1}), first-order longitudinal optical (1LO) phonons (~240 cm^{-1}), and surface optical (SO) phonons (~220 cm^{-1})[49]. The 1LO peaks show a low-frequency shift (~10 cm^{-1}) compared to binary ZnSe (1LO, ~252 cm^{-1}), which is attributed to the effect of ZnTe alloying (1LO, ~210 cm^{-1}). After shell coating, the 1LO peak shifts to a higher frequency in both IPG QDs (from 237.6 cm^{-1} to 240.2 cm^{-1}) and control QDs (from 237.6 cm^{-1} to 244.1 cm^{-1}). The relative intensity of 2LO to 1LO (I_{2LO}/I_{1LO}) ratio increases from 0.52 for the core to 0.74 for the IPG QDs and 0.65 for the control QDs as the QDs grow in size (Supplementary Fig. 7)[50]. The trend is attributed to the confinement of electron and hole wavefunctions. The higher I_{2LO}/I_{1LO} ratio observed in IPG QDs can be explained by the stronger leakage of carrier wavefunction due to the gradient interfacial potential, as discussed in the previous study[51]. Additionally, the linewidth (Γ) of the 1LO peak narrows from 31.0 cm^{-1} to 20.2 cm^{-1} in control QDs and to 15.3 cm^{-1} in IPG QDs. The more pronounced 1LO peak shift ($\Delta\omega = 6.9$ cm^{-1}) and less linewidth narrowing ($\Delta\Gamma = 10.8$ cm^{-1}) observed in control QDs suggest that they experience more significant compressive strain compared to IPG QDs.

To quantify the strain on the ZnSeTe cores, we analyze the relative 1LO phonon shifts ($\frac{\Delta\omega}{\omega}$) of core/IPG QDs and core/ZnSe QDs to estimate relative changes in lattice constant ($\frac{\Delta a}{a}$) using the Grüneisen parameter (γ)[38,39]:

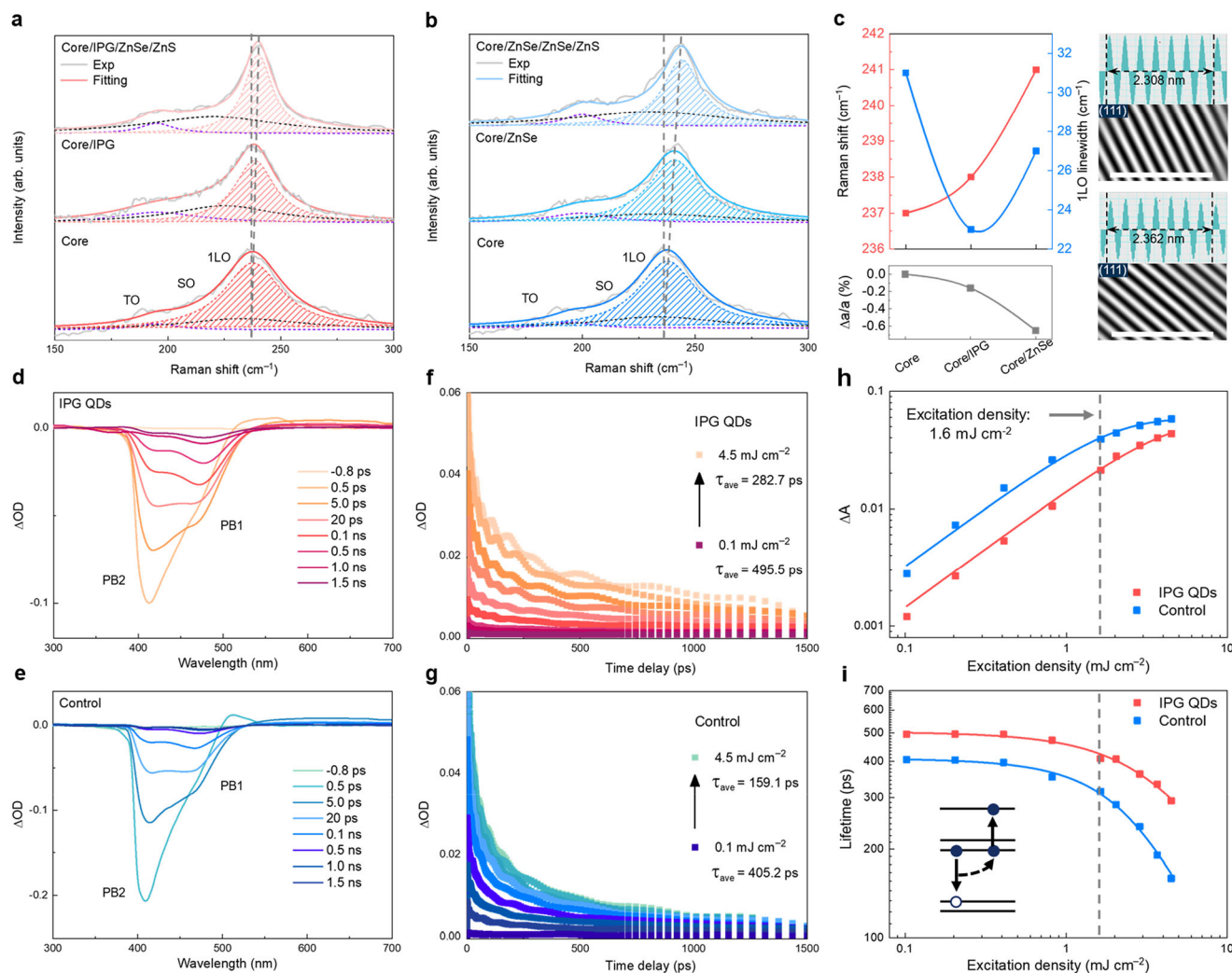$$\frac{\Delta\omega}{\omega} = \left(1 + 3\frac{\Delta a}{a}\right)^{-\gamma} - 1 \qquad (1)$$

Fig. 3 | Lattice strain variations and recombination dynamics. a, b Raman spectra of IPG and control QDs at different stages. The purple dotted line refers to TO mode, the black dotted line refers to SO mode and the red/blue dotted line refers to the 1LO mode of IPG/control QDs. **c,** Raman shift and 1LO linewidth versus different stages of QDs, relative change in lattice constants versus different stages of core, core/IPG, core/ZnSe QDs. The inverse Fourier transform (FFT) images of core/IPG QDs (top) and core/ZnSe QDs (bottom) along [111] are also shown on the right side. The scale bar is 2 nm. **d, e** TA spectra at selected timescales for IPG and control QDs. **f, g** PB1 bleach dynamics of IPG and control QDs at different excitation densities. **h** The bleach amplitude of PB1 as a function of excitation density. **i**, Average lifetime of PB1 dynamics as a function of excitation density for IPG and control QDs. The schematic diagram depicts the Auger recombination under high excitation density.

The $\gamma = 0.85$ is taken in these calculations for both IPG and control QDs[49]. This analysis reveals that both IPG and ZnSe shells introduced compressive strain on the ZnSeTe core, with the ZnSe shell inducing a larger compressive strain ($\frac{\Delta a}{a} = 0.65\%$) compared to IPG shell ($\frac{\Delta a}{a} = 0.16\%$), as shown in Fig. 3c. The lattice constant, derived from the mean interplanar spacing, is 5.71 Å for core/IPG QDs ($d = 3.29$ Å) and 5.84 Å for core/ZnSe QDs ($d = 3.37$ Å) along the [111] crystallographic direction (Fig. 3c and Supplementary Fig. 8). Additionally, the lattice mismatch between the ZnSeTe core and the IPG shell is calculated to be 1.5%, while the mismatch with the ZnSe shell is significantly higher at 3.9%. These findings suggest that the IPG structure effectively alleviates interfacial potential, reduces compressive strain, and minimizes misfit defects, thereby enhancing the luminescent performance of the QDs, which aligns well with the PL characterization results.

To investigate excited-state dynamics and Auger recombination in IPG QDs, we perform ultrafast transient absorption (TA) spectroscopy. The TA spectra for both IPG and control QDs (Fig. 3d, e) reveal two distinct photoinduced bleaching (PB) features at ~410 nm (PB2,

3.02 eV) and 471 nm (PB1, 2.63 eV). PB2 is attributed to carrier filling in the ZnSe shell transition, while PB1 corresponds to state-filling of band-edge in core[34]. At a high excitation density of 4.5 mJ cm^{-2}, the 1S exciton bleach (PB1) in control QDs recovers by about 90% within 0.5 ns, whereas in IPG QDs it recovers by around 60%, indicating that Auger recombination occurs more rapidly in control QDs.

Further investigation using excitation-intensity-dependent TA measurements (varying the excitation density from 0.1 to 4.5 mJ cm^{-2}, Supplementary Fig. 9) focuses on PB1 for detailed kinetic analysis (Fig. 3f, g). All dynamics are well-fitted using a triexponential function, where τ_1, τ_2, and τ_3 represent multiexciton, biexciton, and single-exciton lifetimes, respectively. The fast component (τ_1) is primarily associated with Auger recombination[40,43,45,47,48,52]. For IPG QDs, the average lifetime decreases from 495.5 ps (at 0.1 mJ cm^{-2}) to 282.7 ps (at 4.5 mJ cm^{-2}), while control QDs exhibit a faster decrease, from 405.2 ps to 159.1 ps (Supplementary Tables 3 and 4). Both QD types exhibit similar τ_1 amplitudes up to an excitation intensity of 1.6 mJ cm^{-2}, beyond which control QDs exhibit larger τ_1 amplitudes, indicating faster Auger recombination. We fit the 1S absorption changes at the

different excitation densities using the formula[53,54]:

$$\langle n_{1S} \rangle = 1 - e^{-j_p \sigma_a}\left(1 + j_p \sigma_a / 2\right) \quad (2)$$

where $\langle n_{1S} \rangle$ is the average occupation number of the 1S electron state, the j_p is excitation density and σ_a is the absorption cross-section of a QD. As shown in Fig. 3h, the change in absorption (ΔA) initially increases linearly before saturating at densities above 1.6 mJ cm^{-2}. This behavior aligns with previous studies of ZnSeTe, CuInS$_2$, and CdSe core/shell QDs[40,52,54] and supports our earlier findings.

To quantitatively analyze Auger recombination, we examine the relationship between excitation density and average lifetime. It is widely acknowledged that when the densities of photoexcited electrons and holes are identical, the rate equation for the photocarriers can be simplified to: $1/\tau = \kappa_1 + \kappa_2 n + \kappa_3 n^2$, where κ_1, κ_2, and κ_3 represent the nonradiative single-carrier-trapping rate, radiative bimolecular recombination coefficient, and nonradiative Auger recombination coefficient[42,43], respectively. Global fitting is carried out to simulate the relationship between average lifetime (τ) and excitation density (j_p). The fitting results (Fig. 3i) show that the average lifetime remains constant under low excitation densities but decreases rapidly above 1.6 mJ cm^{-2}, confirming the onset of Auger recombination at high excitation densities. The calculated Auger recombination coefficient for IPG QDs is 9.7×10^{-5} ps^{-1} mJ^{-2} cm^4, which is significantly lower than the 2.2×10^{-4} ps^{-1} mJ^{-2} cm^4 for control QDs (Supplementary Table 5). These results demonstrate that the smoothed interfacial potential in IPG QDs effectively suppresses Auger recombination, indicating a key factor in their enhanced luminescence performance.

Green ZnSeTe-based QLED performance

To verify that reducing defect-assisted nonradiative recombination and Auger recombination in QDs through a smoothed interfacial potential enhances electroluminescence (EL) performance, we fabricate a series of QLEDs. The device structure used in this work is as follows: indium tin oxide (ITO)/poly-(ethylene dioxythiophene): polystyrene sulfonate (PEDOT:PSS) (45 nm)/poly((9,9-dioctyl-fluorenyl-2,7-diyl)-alt-(9-(2-ethylhexyl)-carbazole-3,6-diyl)) (PF8Cz) (40 nm)/ZnSeTe-based core/shell QDs (25 nm)/ZnMgO nanocrystal (60 nm)/Al (100 nm), as depicted in Fig. 4a. The energy levels of QDs are determined using ultraviolet photoemission spectroscopy (UPS) and absorption spectra (Supplementary Fig. 10), while the energy band diagram of QLEDs is provided in Supplementary Fig. 11. The large potential barrier and high electron mobility of ZnMgO lead to electron accumulation at the interface[2,10,24]. The introduction of the IPG configuration enhances carrier injection into the IPG QDs compared to control QDs, as shown by capacitance-voltage curves (Supplementary Fig. 12). As the applied voltage increases, carriers are injected and accumulate in the QLEDs, which is reflected by a slight initial increase in capacitance followed by a rapid rise around 2.2 V. The peak capacitance of IPG QLEDs occurs at a lower voltage and shows a smaller value than that of control QLEDs, indicating a lower carrier injection barrier and charge accumulation.

The current density-voltage-luminance (*J-V-L*) characteristics (Fig. 4b) demonstrate that QLEDs based on IPG QDs exhibit a low turn-on voltage of 2.2 V (driving voltage at a luminance of 1 cd m^{-2}), and a peak brightness of 52,040 cd m^{-2} at a low driving voltage of 5.4 V. This high brightness at such a low driving voltage far exceeds the brightness of the most heavy-metal-free green QLEDs (such as InP-based QLEDs and carbon QLEDs)[20,23–26,28]. In contrast, the QLEDs based on control QDs show a lower peak brightness of 35,000 cd m^{-2}. As the driving voltage increased from 2.0 V to 6.0 V, the EL intensity of the IPG QLEDs rose rapidly and remained stable, without any shift in the EL spectra at 520 nm, even under high bias voltage (Fig. 4c, Supplementary Fig. 13a). The slight discrepancy between EL and PL peak can be primarily attributed to two factors: Förster resonance energy transfer (FRET) and the electric field-induced Stark effect. Given that the EL peak consistently remains at 520 nm across various voltages with no observable spectral shifts, this discrepancy in PL peak can be attributed to FRET, as observed in the QDs film PL (Supplementary Fig. 13b).
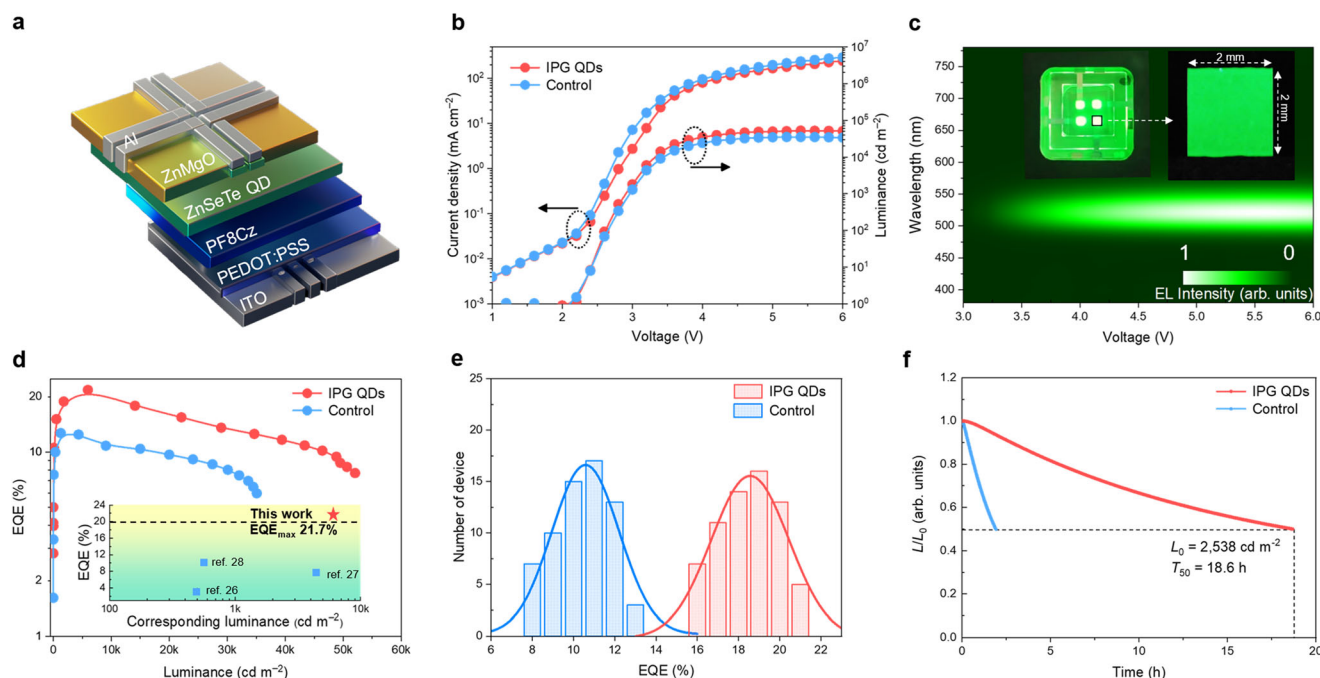

Fig. 4 | Device structure and performance of QLEDs. a Device architecture of the green QLED. **b** Current density-voltage-luminance characteristics of the green QLEDs based on control and IPG QDs. **c** Two-dimensional (2D) map of drive-voltage-dependent EL spectra of IPG QLED. The photo of operating device is shown in inset with a pixel size of 4 mm². **d** Corresponding EQE-luminance characteristics (inset: summary of the reported ZnSeTe green QLEDs performance on the basis of maximum EQE and the corresponding luminance). **e** Histograms of the peak EQEs for control and IPG QDs, each measured with over 60 devices. **f** Operational stability of QLEDs under constant current of 1.22 mA for IPG and control QLEDs.

Notably, the QLEDs based on IPG QDs achieve a maximum EQE of 21.7% at a high luminance of 5963 cd m^{-2} (Fig. 4d), with a corresponding current efficiency (CE) of 75.7 cd A^{-1} (Supplementary Fig. 14). In comparison, the QLEDs based on control QDs show a maximum EQE of 13.0% at a luminance of 1290 cd m^{-2}. This high EQE at such high luminance reflects the effect of suppression in Auger recombination, enabled by the smoothed interfacial potential in the IPG QDs. This performance represents the highest EQE for green ZnSeTe-based QLEDs to the best of our knowledge (in the inset of Fig. 4d and Supplementary Table 6)[26–28].

The reproducibility of these devices is demonstrated by the distribution of EQE values obtained from over 60 devices, as shown in Fig. 4e. The average EQE for the control QLEDs is 10.5%, whereas QLEDs based on IPG QDs achieve an average EQE of 18.6%. This demonstrates consistent performance improvement in the IPG QLEDs, highlighting the effectiveness of the IPG design in enhancing efficiency across multiple devices. Since the Auger process significantly impacts device operational stability[18,42], the operational stability of QLEDs is evaluated at high luminance. The lifetimes of QLEDs are shown in Fig. 4f. The T_{50} lifetime is measured at a constant current of 1.22 mA. The QLEDs based on IPG QDs exhibit a T_{50} lifetime of 18.6 h at an initial luminance of 2538 cd m^{-2}, corresponding to 99.4 h @ 1000 cd m^{-2} ((L_0)^n × T_{50} = constant, where n = 1.8 is acceleration factor). In contrast, the control QLED exhibit a much shorter lifetime, with T_{50} being 1.9 h at 2941 cd m^{-2} (corresponding to T_{50} = 13.3 h at 1000 cd m^{-2}). These results demonstrate that the suppression of Auger recombination through the engineering of the interfacial potential plays a critical role in enhancing both the efficiency and stability of QLEDs. The substantial improvement in both performance and operational lifetime indicates the great potential of IPG QDs for practical, long-lasting applications in high-performance displays and lighting technologies.

Discussion

In conclusion, we have successfully developed efficient ZnSeTe green QLEDs by controlling the interfacial potential. The proposed IPG structure design mitigates the lattice strain in ZnSeTe QDs and reduces their nonradiative Auger recombination rate. Time-dependent and excitation-density-dependent TA kinetics reveal that Auger recombination in IPG QDs is reduced by an order of magnitude compared to that in control QDs with an abrupt interfacial potential structure. As a result, the IPG QDs achieve an impressive PL QY of up to 95%, with a narrow linewidth of 38 nm. Furthermore, the QLEDs based on IPG QDs exhibit a high EQE of 21.7% and a brightness of 52,040 cd m^{-2}, alongside a long T_{50} lifetime of 99.4 h at 1000 cd m^{-2}. This work represents a significant advancement toward the use of eco-friendly QDs-based QLEDs for display and lighting applications.

Methods
Materials
Zinc chloride (ZnCl$_2$, 99.99%), zinc acetate (Zn(OAc)$_2$, 99.99%), sulfur powder (S, 99.999%), selenium powder (Se, 99.999%), diethylzinc (DEZ; 1.0 M in ODE), trioctylphosphine (TOP, 97%), tellurium (99.99%), tri-n-octylamine (TOA, 90%), oleylamine (OLA, 90%), oleic acid (OA, 90%), 1-octadecene (ODE, 90%), heptane (90%), octane (99%), Palmitic acid (PA, 90%), 1-dodecanethiol (DDT, 98%), diphenylphosphine (DPP), HF (48%), tris[2-(diphenylphosphino)ethyl]phosphine were purchased from Aladdin. Poly-(ethylene dioxythiophene): polystyrene sulfonate (PEDOT:PSS), poly((9,9-dioctylfluorenyl-2,7-diyl)-alt-(9-(2-ethylhexyl)-carbazole-3,6-diyl)) (PF8Cz), and zinc magnesium oxide (ZnMgO) nanocrystals which were purchased from Suzhou Xingshuo Nanotech Co., Ltd All chemicals were used without any purification.

Preparation of precursors
Zn(OA)$_2$ precursor: a 1000 mL flask was charged with a mixture consisting of 500 mmol of Zn(AC)$_2$, 310 mL of OA, 140 mL of TOP, and 140 mL of TOA. This mixture was heated to 120 °C and underwent degassing for 1 h. Subsequently, it was heated to 300 °C and kept boiling for 20 min. Selenium precursor: 500 mmol of selenium powder was blended with 250 mL of TOP and stirred continuously until a clear solution was achieved. Sulfur precursor: 500 mmol of sulfur powder was blended with 250 mL of TOP and stirred continuously until a clear solution was achieved. Zn(OLA)$_2$ precursor: a 1000 mL flask was filled with a mixture of 290 mmol of Zn(AC)$_2$, 120 mL of OLA, and 500 mL of ODE. The mixture was then heated to 120 °C and degassed for 1 h. ZnCl$_2$-OLA precursor: ZnCl$_2$ (25 mmol) and OLA (50 mL) were loaded into a 100 mL flask, heated to 120 °C, and degassed for 1 h.

Synthesis of IPG and control QDs
For the synthesis of core, 0.256 g of PA (1 mmol), 2.5 mL of OLA, and 10 mL of TOA were added into a 100 mL three-neck flask. The mixture was heated to 120 °C and degassed for 2 h. The temperature was then raised to 240 °C under a N$_2$ flow. At this point, DPP (2 mmol), TOP-Se (2 M, 0.48 mmol), TOP-Te (0.1 M, 0.12 mmol), and DEZ (1 M, 1.2 mmol) were injected into the flask, and the reaction was maintained for 30 min to grow ZnSeTe cores. Subsequently, 0.1 mL ZnCl$_2$-OLA (0.5 M) and 1.0 mL of diluted HF (1 wt%) were injected into the flask with carefully controlled N$_2$ flow.

For the growth of IPG shell, after synthesizing of ZnSeTe cores, the temperature was increased to 280 °C, and 4 mL of Zn(OA)$_2$ was added to the flask. Then, over a period of 0.7 h, 0.2 mL Se precursor and 0.45 mL Te precursor were injected using a syringe pump to grow the IPG shell. For the control QDs, the same initial steps were followed, with the temperature raised to 280 °C, and 4 mL of Zn(OA)$_2$ added. However, only 0.2 mL of Se precursor was injected over 0.7 h using a syringe pump, without the addition of Te, to form the standard core/shell structure.

Growth of ZnSe/ZnS shell: After the formation of IPG or control shell, the temperature was increased to 310 °C. At this temperature, 10 mL Zn(OA)$_2$ and 2.0 mL Se precursor were injected over 1 h. Following this, the temperature was maintained at 310 °C, and 10 mL of Zn(OA)$_2$ and 2.0 mL of S precursor were injected over another 1 h to coat the ZnS shell. The reaction was then cooled to 250 °C, and 20 mL of Zn(OLA)$_2$ and 4 mL of S precursor were injected over 0.5 h, completing the shell coating process. After the reaction, the flask was cooled to room temperature. The resulting QDs were dispersed in heptane and centrifuged at 1791 × g for 5 min. The supernatant was purified with ethanol and centrifuged again at 1791 × g for 5 min for twice. The supernatant solution was discarded, and the precipitate was dispersed in 10 mL octane for further characterization.

Fabrication of green QLEDs
The QLEDs were constructed based on the indium tin oxide (ITO)/PEDOT:PSS/PF8Cz/QDs/ZnMgO/Al structure. Except for the Al cathode deposited by thermal evaporation under vacuum, the remaining layers were spin-coated onto ITO glasses. The ITO-coated glasses underwent successive ultrasonic cleaning in washing water, deionized water, acetone, and isopropanol, each for 30 min, and then 15-min ultraviolet ozone cleaning. The PEDOT:PSS (4083) solution was spin-coated onto ITO glasses at 3000 rpm for 30 s and annealed at 130 °C for 20 min in air. Subsequently, the PF8Cz solution (8 mg mL^{-1} dissolved in trimethylbenzene) was spin-coated at 3000 rpm for 30 s and annealed at 130 °C for 20 min in a glove box. Next, the QDs solution (16 mg mL^{-1} in octane) was spin-coated at 3000 rpm for 30 s and annealed at 80 °C for 5 min in the glove box. After that, the ZnMgO solution (20 mg mL^{-1} in ethanol) was spin-coated at 3000 rpm for 30 s, and the resulting films were annealed at 80 °C for 10 min. After that, the devices were moved to a vacuum evaporator with a vacuum level of 5 × 10^{-4} Pa to deposit a 100-nm-thick Al cathode at a speed of 5 nm s^{-1}. Some devices were fabricated using

Mesolight Inc's "Hands-Liberated Diode (HLD-V1.0) Automated Integration System" for reproducibility verification, which can automatically process PEDOTS:PSS/PF8Cz/QDs/ZnO layers (spin-coating & annealing). In the glove box, all the devices were encapsulated using commercially available ultraviolet-curable resin for subsequent characterization.

PL and structure characterization
PL spectra, PL QY, and TRPL of QDs were characterized using a Horiba Fluorolog®-3 system equipped with a Synapse PLUS CCD detection system, an F-3029 integrating sphere accessory, the Quanta-φ, and a 450 W Xenon lamp along with associated accessories. For all samples, the excitation wavelength was set to 450 nm. Absorption spectra were measured with a UV-vis spectrophotometer (PerkinElmer Instruments, Lambda 750). The QD films were prepared by spin-coating the QD solution on a cleaned glass at 2000 rpm for 15 s. X-ray diffraction measurements were performed over a 2θ range of 20°–70°, using a Cu Kα ($\lambda = 1.5405$ Å) rotating anode with a SMARTLAB 3 kW X-ray diffractometer (Rigaku Corporation). TEM images were acquired using a FEI Talos F200X G2 microscope operating at 200 kV. HAADF STEM images, EDS elemental mapping, and line scan images of QDs were measured using a Thermo Scientific Spectra 300 microscope. The VBM of QDs was estimated using a UV photoelectron spectrometer (Thermofisher ESCALAB 250Xi) with a He I (21.2 eV) photon source. XPS data were obtained using a Thermo Scientific K-Alpha system with a monochromatic Al K$\alpha 1$ X-ray source ($h\nu = 1486.6$ eV, where h is the Planck constant and ν is the frequency of the X-ray photons).

Raman characterization
Raman spectra of the QDs were performed using a confocal Raman spectral system (alpha 300 R) with a 532 nm excitation wavelength and a 50× objective lens at room temperature. The Raman spectra were calibrated using a standard Si wafer prior to the measurements. The prepared samples were mounted on piezoelectric stages, and the laser light was focused on the sample using a lens with a numerical aperture of 0.82, producing a spot ~1 μm in diameter. The emitted light was collected by the same objective and scattered by a 0.75 m spectrometer, equipped with 150 and 1800 lines/mm gratings and a CCD camera.

TA characterization and analyses
Femtosecond pump-probe setup. A Ti: Sapphire laser (Coherent Libra) was employed to generate femtosecond pulses at 800 nm. These pulses were directed towards an optical parametric amplifier (OperA Solo from Coherent), yielding femtosecond pulses (~50 fs, 1 kHz) with wavelengths spanning from 400 to 2500 nm and a maximum average power of around 500 mW. The idler light served as the pump light. The probe light, a white-light continuum, was generated by focusing the 800 nm laser beam onto a sapphire plate. The electronic signal from the detector was amplified by a lock-in amplifier (Stanford Research Systems: SR830) and synchronized with the laser's trigger frequency.

TA fitting analysis. The QD populations were modeled using a Poisson distribution, given that pump wavelength saturation was negligible. The average QD population, $\langle N \rangle$, was described by: $P(N) = \langle N \rangle^N e^{-\langle N \rangle}/N!$. The change in 1S absorption (ΔA) is proportional to the population of the 1S electron state: $\triangle A \propto \langle n_{1S} \rangle$, which $\langle n_{1S} \rangle$ represents the average occupation number of the 1S electron state. Considering the twofold spin degeneracy for the 1S electron state, they $\langle n_{1S} \rangle$ can be expressed as:

$$\langle n_{1S} \rangle = 1 - e^{-\langle N \rangle} \left(1 + \langle N \rangle /2 \right) \tag{3}$$

here, the $\langle N \rangle$ is proportional to the pump fluence (j_p) and can be expressed as: $\langle N \rangle = j_p \sigma_a$, where σ_a is the absorption cross-section of the QD. Thus, the $\langle n_{1S} \rangle$ can be expressed as:

$$\langle n_{1S} \rangle = 1 - e^{-j_p \sigma_a} \left(1 + j_p \sigma_a /2 \right) \tag{4}$$

The changes in 1S absorption and excitation density were fitted using Eq. (4).

QLED characterization
A Keithley 2400 source meter and a spectrometer (Ocean Optics, QE65000) were utilized to measure the current density-voltage (J–V) characteristics and EL spectra of the QLEDs. A calibrated spectral scanning colorimeter (Photo Research 655) was employed to measure the luminance of the QLEDs. The EQE of the QLEDs was calculated according to the formula:

$$\eta = \frac{\pi Le}{KmhcJ} \bullet \frac{\int I(\lambda)\lambda d\lambda}{\int I(\lambda)V(\lambda)d\lambda} \tag{5}$$

where e represents the electron charge, h stands for the Planck constant, c is the velocity of light, and $Km = 683$ lm W^{-1} is the maximum luminous efficacy. J refers to the current density, $I(\lambda)$ refers to the relative electroluminescence intensity at wavelength λ, $V(\lambda)$ is the normalized photonic spectral response function, and L represents the luminance.

Data availability
The data that support the findings of this study are available from the corresponding author upon request.

References
1. Shirasaki, Y., Supran, G. J., Bawendi, M. G. & Bulović, V. Emergence of colloidal quantum-dot light-emitting technologies. *Nat. Photon.* **7**, 13–23 (2012).
2. Dai, X. et al. Solution-processed, high-performance light-emitting diodes based on quantum dots. *Nature* **515**, 96–99 (2014).
3. Yoo, J. et al. Highly efficient printed quantum dot light-emitting diodes through ultrahigh-definition double-layer transfer printing. *Nat. Photon.* **18**, 1105–1112 (2024).
4. Vasilopoulou, M. et al. Efficient colloidal quantum dot light-emitting diodes operating in the second near-infrared biological window. *Nat. Photon.* **14**, 50–56 (2019).
5. Dai, X., Deng, Y., Peng, X. & Jin, Y. Quantum-dot light-emitting diodes for large-area displays: towards the dawn of commercialization. *Adv. Mater.* **29**, 1607022 (2017).
6. Meng, T. et al. Ultrahigh-resolution quantum-dot light-emitting diodes. *Nat. Photon.* **16**, 297–303 (2022).
7. Li, M. et al. Ultrabright and stable top-emitting quantum-dot light-emitting diodes with negligible angular color shift. *Nat. Commun.* **15**, 5161 (2024).
8. Xu, H. et al. Dipole–dipole-interaction-assisted self-assembly of quantum dots for highly efficient light-emitting diodes. *Nat. Photon.* **18**, 186–191 (2024).
9. Gao, Y. et al. Minimizing heat generation in quantum dot light-emitting diodes by increasing quasi-Fermi-level splitting. *Nat. Nanotechnol.* **18**, 1168–1174 (2023).
10. Deng, Y. et al. Solution-processed green and blue quantum-dot light-emitting diodes with eliminated charge leakage. *Nat. Photon.* **16**, 505–511 (2022).
11. Shen, H. et al. Visible quantum dot light-emitting diodes with simultaneous high brightness and efficiency. *Nat. Photon.* **13**, 192–197 (2019).
12. Xing, S. et al. Energy-efficient perovskite LEDs with rec *2020* compliance. *ACS Energy Lett.* **9**, 3643–3651 (2024).
13. Kim, J. S. et al. Ultra-bright, efficient and stable perovskite light-emitting diodes. *Nature* **611**, 688–694 (2022).

14. Yuan, S. et al. Efficient blue electroluminescence from reduced-dimensional perovskites. *Nat. Photon.* **18**, 425–431 (2024).

15. Yuan, F. et al. Bright and stable near-infrared lead-free perovskite light-emitting diodes. *Nat. Photon.* **18**, 170–176 (2024).

16. Zhao, J. et al. Efficient CdSe/CdS quantum dot light-emitting diodes using a thermally polymerized hole transport layer. *Nano Lett.* **6**, 463–467 (2006).

17. Won, Y.-H. et al. Highly efficient and stable InP/ZnSe/ZnS quantum dot light-emitting diodes. *Nature* **575**, 634–638 (2019).

18. Bian, Y. et al. Efficient green InP-based QD-LED by controlling electron injection and leakage. *Nature* **635**, 854–859 (2024).

19. Kim, T. et al. Efficient and stable blue quantum dot light-emitting diode. *Nature* **586**, 385–389 (2020).

20. Yu, P. et al. Highly efficient green InP-based quantum dot light-emitting diodes regulated by inner alloyed shell component. *Light. Sci. Appl.* **11**, 162 (2022).

21. Bi, Y. et al. Reducing emission linewidth of pure-blue ZnSeTe quantum dots through shell engineering toward high color purity light-emitting diodes. *Small* **19**, 2303247 (2023).

22. Lee, S.-H. et al. Heterostructural tailoring of blue ZnSeTe quantum dots toward high-color purity and high-efficiency electro-luminescence. *Chem. Eng. J.* **429**, 132464 (2022).

23. Chao, W.-C. et al. High efficiency green InP quantum dot light-emitting diodes by balancing electron and hole mobility. *Commun. Mater.* **2**, 96 (2021).

24. Moon, H. et al. Composition-tailored ZnMgO nanoparticles for electron transport layers of highly efficient and bright InP-based quantum dot light emitting diodes. *Chem. Commun.* **55**, 13299–13302 (2019).

25. Liu, P. et al. Green InP/ZnSeS/ZnS core multi-shelled quantum dots synthesized with aminophosphine for effective display applications. *Adv. Funct. Mater.* **31**, 2008453 (2021).

26. Heo, H. S. et al. Enhanced fluorescence in green ZnSeTe quantum dots using gradient layer technique. *Adv. Opt. Mater.* **13**, 2402215 (2025).

27. Lee, S.-H. et al. ZnSeTe quantum dots as an alternative to InP and their high-efficiency electroluminescence. *Chem. Mater.* **32**, 5768–5775 (2020).

28. Yoon, S.-Y. et al. Highly emissive green ZnSeTe quantum dots: effects of core size on their optical properties and comparison with InP counterparts. *ACS Energy Lett.* **8**, 1131–1140 (2023).

29. Pust, P., Schmidt, P. J. & Schnick, W. A revolution in lighting. *Nat. Mater.* **14**, 454–458 (2015).

30. Chen, B., Li, D. & Wang, F. InP quantum dots: synthesis and lighting applications. *Small* **16**, 2002454 (2020).

31. Wu, K., Lim, J. & Klimov, V. I. Superposition principle in auger recombination of charged and neutral multicarrier states in semiconductor quantum dots. *ACS Nano* **11**, 8437–8447 (2017).

32. Cragg, G. E. & Efros, A. L. Suppression of auger processes in confined structures. *Nano Lett.* **10**, 313–317 (2009).

33. World Health Organization IARC. Monographs on the evaluation of the carcinogenic risk of chemicals to humans: Cobalt in hard metals and cobalt sulfate, Gallium Arsenide, Indium Phosphide and Vanadium Pentoxide. **86**, (IARC, 2006).

34. Huang, Z. et al. Broadband tunable optical gain from ecofriendly semiconductor quantum dots with near-half-exciton threshold. *Nano Lett.* **23**, 4032–4038 (2023).

35. Kim, Y.-H. et al. Compositional and heterostructural tuning in red-emissive ternary ZnSeTe quantum dots for display applications. *ACS Appl. Nano Mater.* **6**, 19947–19954 (2023).

36. Wang, X. et al. Non-blinking semiconductor nanocrystals. *Nature* **459**, 686–689 (2009).

37. Lee, Y. et al. Effectual interface and defect engineering for Auger recombination suppression in bright InP/ZnSeS/ZnS quantum dots. *ACS Appl. Mater. Interfaces* **14**, 12479–12487 (2022).

38. Zhang, J., Li, C., Li, J. & Peng, X. Synthesis of CdSe/ZnSe core/shell and CdSe/ZnSe/ZnS core/shell/shell nanocrystals: surface-ligand strain and CdSe–ZnSe lattice strain. *Chem. Mater.* **35**, 7049–7059 (2023).

39. Van Avermaet, H. et al. Full-spectrum InP-based quantum dots with near-unity photoluminescence quantum efficiency. *ACS Nano* **16**, 9701–9712 (2022).

40. Huang, Z. et al. Deciphering ultrafast carrier dynamics of eco-friendly ZnSeTe-based quantum dots: toward high-quality blue-green emitters. *J. Phys. Chem. Lett.* **12**, 11931–11938 (2021).

41. Kim, S. et al. Efficient blue-light-emitting Cd-free colloidal quantum well and its application in electroluminescent devices. *Chem. Mater.* **32**, 5200–5207 (2020).

42. Jiang, Y. et al. Reducing the impact of Auger recombination in quasi-2D perovskite light-emitting diodes. *Nat. Commun.* **12**, 336 (2021).

43. Yamada, Y., Yasuda, H., Tayagaki, T. & Kanemitsu, Y. Temperature dependence of photoluminescence spectra of nondoped and electron-doped $SrTiO_3$: crossover from auger recombination to single-carrier trapping. *Phys. Rev. Lett.* **102**, 247401 (2009).

44. Wu, B. et al. Excited-state regulation in eco-friendly ZnSeTe-based quantum dots by cooling engineering. *Sci. China Mater.* **65**, 1569–1576 (2022).

45. Cai, W. et al. Emission mechanism of bright and eco-friendly ZnSeTe quantum dots. *Adv. Opt. Mater.* **12**, 2301970 (2023).

46. Gu, Y. et al. Zn–Se–Te multilayers with submonolayer quantities of Te: type-II quantum structures and isoelectronic centers. *Phys. Rev. B* **71**, 045340 (2005).

47. Chang, J. H. et al. Impact of morphological inhomogeneity on excitonic states in highly mismatched alloy $ZnSe_{1-x}Te_x$ nanocrystals. *J. Phys. Chem. Lett.* **13**, 11464–11472 (2022).

48. Imran, M. et al. Molecular-additive-assisted tellurium homogenization in ZnSeTe quantum dots. *Adv. Mater.* **35**, 2303528 (2023).

49. Boldt, K. Raman spectroscopy of colloidal semiconductor nanocrystals. *Nano Futures* **6**, 012003 (2022).

50. Lu, S. H., Chen, T. F., Wang, A. J., Wu, Z. L. & Wang, Y. S. Lattice and optical property evolution of ultra-small ZnS quantum dots grown from a single-source precursor. *Appl. Surf. Sci.* **299**, 116–122 (2014).

51. Zhang, Q. et al. Exciton-phonon coupling in individual ZnTe nanorods studied by resonant Raman spectroscopy. *Phys. Rev. B* **85**, 085418 (2012).

52. Zhu, H., Song, N., Rodríguez-Córdoba, W. & Lian, T. Wave function engineering for efficient extraction of up to nineteen electrons from one CdSe/CdS quasi-type II quantum dot. *J. Am. Chem. Soc.* **134**, 4250–4257 (2012).

53. Nanda, J. et al. Absorption cross sections and Auger recombination lifetimes in inverted core-shell nanocrystals: implications for lasing performance. *J. Appl. Phys.* **99**, 034309 (2006).

54. Sun, J. et al. Ultrafast carrier dynamics in $CuInS_2$ quantum dots. *Appl. Phys. Lett.* **104**, 023118 (2014).

Acknowledgements

Author contributions

J.Z. and Y.W. supervised the research. S.C. and Y.B. conceptualized and designed the experiments. Y.B. performed most of the experiments and analyzed the data. J.S. conducted the TA measurements. B.Z., X.Y., J.Z.,

and Q.L. provided technical support and advice. S.C., Y.B., and J.Z. wrote and revised the manuscript. All authors contributed to the analysis and discussion of the experimental results.

Competing interests

The authors declare no competing interests.

Additional information